*Int. J. Heat Mass Transfer.* Vol. 34, No. 10, pp. 2603–2615, 1991
Printed in Great Britain

0017–9310/91 $3.00+0.00


# Efficiency of transient contaminant removal from a slot ventilated enclosure

J. L. LAGE and A. BEJAN
Department of Mechanical Engineering and Materials Science, Duke University, Durham, NC 27706, U.S.A.

and

R. ANDERSON
SERI, Building Energy Technology Program, 1617 Cole Boulevard, Golden, CO 80401, U.S.A.

(*Received* 9 *August* 1990 *and in final form* 9 *November* 1990)

**Abstract**—This paper reports the results of a fundamental study of the transient removal of a contaminant from a two-dimensional enclosure with one inlet and one outlet. The evolution of the flow and concentration fields are simulated numerically using Jones and Launder's low Reynolds number $k$–$\varepsilon$ model. The Reynolds number is varied over the range 5–5000, where $Re$ is based on the jet inlet width. The effectiveness of this forced convection mass transfer process is documented quantitatively in terms of a ventilation efficiency and a critical concentration decay time. The relationship between these quantitative performance parameters, the Reynolds number and the ventilation jet orientation, is reported. It is shown that significant gains in ventilation efficiency (or a shortening of the critical concentration decay time) can be made by properly orienting and positioning the inlet and outlet ports relative to each other and to the enclosure. The numerical ventilation efficiency results are summarized by a compact analytical expression based on a theoretical two-zone model of the enclosure flow.

## 1. INTRODUCTION

HEAT AND mass transfer processes in enclosures have occupied a central place on the research stage for the past two decades. Their prominence has been due to interest in energy conservation and chemical reactor kinetics. During the last five years or so, we have witnessed a resurgence of interest in enclosure flows, as a result of concern over the quality of indoor air. A 'healthy' building must supply adequate levels of outside air and control indoor contaminants, in addition to saving energy. The efficiency with which these tasks are accomplished determines the associated energy costs.

The present study examines the dependence of ventilation efficiency upon jet orientation, by focusing on the transient removal of a uniformly distributed contaminant, from an enclosure with one inlet and one outlet. Of primary engineering interest is the critical decay time, or the time needed to remove the original contaminant. The flow conditions of most interest are turbulent, therefore the focus is on the low Reynolds number range of the turbulent regime.

In what follows, we illustrate the time-dependent development of the flow and concentration fields during through-flow ventilation. For the engineer, we report the relationship between the critical clean-up time and key parameters such as the Reynolds number and the enclosure geometry. We also develop a compact analytical expression that summarizes the ventilation efficiency information generated by this study.

## 2. MODEL

Consider the two-dimensional rectangular enclosure illustrated in Fig. 1. The mixture that fills and flows through this enclosure is a Newtonian fluid with nearly constant density $\rho$ and viscosity $\mu$. The mass diffusivity $\mathscr{D}$ of the diffusing species of interest (concentration $c$) is also constant.

The governing equations are the Reynolds-averaged equations for mass continuity, momentum and species conservation. In these equations, the averaging is taken only over the high frequencies associated with turbulent fluctuations, so that the momentum, and concentration equations retain the time-derivative terms accounting for the much slower development of the purging flow initiated through the enclosure. As indicated in Fig. 1, the 'clean' through-flow $\dot{m}$ is started at the time $t = 0$, when the cavity fluid is motionless and uniformly contaminated with the species of interest, whose initial concentration is $c_0$.

The dimensionless set of time-averaged mass, momentum and species concentration equations is

$$\frac{\partial U}{\partial X}+\frac{\partial V}{\partial Y}=0 \tag{1}$$

$$\frac{\mathrm{D}U}{\mathrm{D}\tau}=-\frac{\partial P}{\partial X}+\frac{1}{Re}\nabla^2 U+2\frac{\partial}{\partial X}\left(\frac{1}{Re^*}\frac{\partial U}{\partial X}\right)+\frac{\partial}{\partial Y}\left[\frac{1}{Re^*}\left(\frac{\partial V}{\partial X}+\frac{\partial U}{\partial Y}\right)\right] \tag{2}$$

## NOMENCLATURE

| | |
|---|---|
| $a_{1,2,k}$ | constants, equation (19) |
| $A$ | empirical coefficient, Table 2 |
| $b_1$ | empirical factor, equation (32) |
| $\tilde{b}_{1,2}$ | dimensionless factors, equation (36) |
| $B$ | source term, equation (11) |
| $c, C$ | concentration† |
| $C_i$ | average concentration in the 'roll' region, Fig. 10, bottom |
| $\mathscr{D}$ | mass diffusivity |
| $E$ | dimensionless rate of dissipation of turbulence kinetic energy |
| $f_{1,2}$ | dimensionless factors, equations (16) and (17) |
| $G$ | turbulence kinetic energy due to viscous stresses, equation (10) |
| $h$ | width of inlet and outlet ports |
| $H$ | height of enclosure |
| $k, K$ | turbulence kinetic energy† |
| $L$ | length of enclosure |
| $m$ | empirical exponent, Table 2 |
| $\dot{m}$ | mass flow rate, Fig. 1 |
| $p, P$ | pressure† |
| $P_K$ | turbulence kinetic energy due to Reynolds shear stresses, equation (9) |
| $Re$ | Reynolds number based on inlet width, equation (14) |
| $Re^*$ | Reynolds number based on eddy viscosity, equation (15) |
| $Re_t$ | turbulence Reynolds number, equation (18) |
| $Sc$ | molecular Schmidt number, $\nu/\mathscr{D}$ |
| $t$ | time |
| $t_c$ | critical concentration decay time |
| $u, U$ | horizontal velocity component† |
| $u_{in}$ | average inlet velocity |
| $v, V$ | vertical velocity component† |
| $x, X$ | horizontal coordinate† |
| $y, Y$ | vertical coordinate.† |

Greek symbols

| | |
|---|---|
| $\varepsilon$ | rate of dissipation of turbulence kinetic energy |
| $\eta_d$ | displacement efficiency, equation (24) |
| $\nu$ | kinematic viscosity |
| $\nu_t$ | turbulence kinematic viscosity |
| $\rho$ | density |
| $\sigma_C$ | turbulence Schmidt number |
| $\sigma_{E,K}$ | turbulence Prandtl numbers |
| $\tau$ | dimensionless time, equation (12) |
| $\tau^*$ | dimensionless time, equation (22) |
| $\tau_c^*$ | critical dimensionless time, equation (26) |
| $\Psi$ | dimensionless streamfunction. |

Subscripts

| | |
|---|---|
| in | inlet |
| out | outlet |
| 0 | initial. |

Superscript

| | |
|---|---|
| $\bar{}$ | space averaged. |

† Capital letters indicate non-dimensionalized variables.

$$\frac{DV}{D\tau} = -\frac{\partial P}{\partial Y} + \frac{1}{Re}\nabla^2 V + \frac{\partial}{\partial X}\left[\frac{1}{Re^*}\left(\frac{\partial V}{\partial X} + \frac{\partial U}{\partial Y}\right)\right] + 2\frac{\partial}{\partial Y}\left(\frac{1}{Re^*}\frac{\partial V}{\partial Y}\right) \quad (3)$$

$$\frac{DC}{D\tau} = \frac{1}{Re\,Sc}\nabla^2 C + \nabla\cdot\left(\frac{\nabla C}{Re^*\,\sigma_C}\right). \quad (4)$$

The eddy diffusivity was calculated based on Jones and Launder's [1] low-Reynolds number $k$–$\varepsilon$ model, which consists of solving two additional equations

$$\frac{DK}{D\tau} = \frac{1}{Re}\nabla^2 K + \nabla\cdot\left(\frac{\nabla K}{Re^*\,\sigma_K}\right) + P_K + G - Re\,E \quad (5)$$

$$\frac{DE}{D\tau} = \frac{1}{Re}\nabla^2 E + \nabla\cdot\left(\frac{\nabla E}{Re^*\,\sigma_E}\right) + a_k P_K\frac{E}{K} + B - a_1 f_1\,Re\frac{E^2}{K} \quad (6)$$

in which

$$\frac{D}{D\tau} = \frac{\partial}{\partial\tau} + U\frac{\partial}{\partial X} + V\frac{\partial}{\partial Y} \quad (7)$$

$$\nabla = \frac{\partial}{\partial X}\mathbf{i} + \frac{\partial}{\partial Y}\mathbf{j} \quad (8)$$

and

$$P_K = \frac{1}{Re^*}\left\{2\left[\left(\frac{\partial U}{\partial X}\right)^2 + \left(\frac{\partial V}{\partial Y}\right)^2\right] + \left(\frac{\partial U}{\partial X} + \frac{\partial V}{\partial Y}\right)^2\right\} \quad (9)$$

$$G = -\frac{2}{Re}\left[\left(\frac{\partial\sqrt{K}}{\partial X}\right)^2 + \left(\frac{\partial\sqrt{K}}{\partial Y}\right)^2\right] \quad (10)$$

$$B = \frac{2}{Re^2\,Re^*}\left[\left(\frac{\partial^2 U}{\partial Y^2}\right)^2 + \left(\frac{\partial^2 V}{\partial X^2}\right)^2\right]. \quad (11)$$

Physically, $P_K$ accounts for the production of kinetic energy by Reynolds shear stresses, while $G$ represents the kinetic energy generated by viscous stresses. As

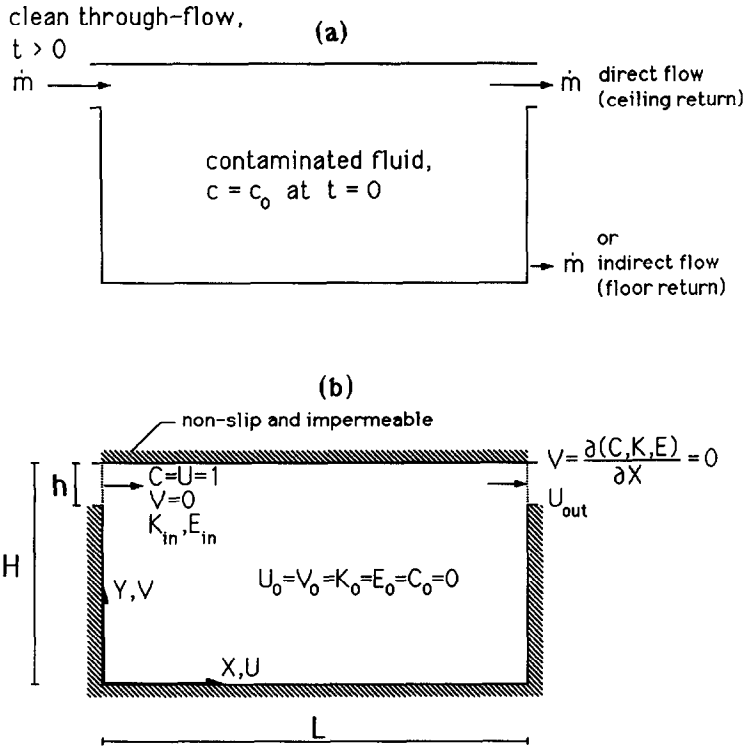


FIG. 1. Two-dimensional enclosure with sudden through-flow, and the dimensionless initial and boundary conditions: (a) inlet and outlet locations; (b) boundary conditions.

indicated by Jones and Launder, equation (11) does not have a physical interpretation: $B$ is a source term required in order to match turbulence kinetic energy to experimental data. Jones and Launder's model [1] is similar to that of Lam and Bremhorst [2], in which the $G$ and $B$ terms do not appear in equations (5) and (6). Although Lam and Bremhorst's modification of the $k$–$\varepsilon$ model is a little bit simpler, we chose Jones and Launder's model because it is used more widely in computational fluid dynamics.

Equations (1)–(11) have been written in terms of the following dimensionless variables:

$$(X, Y) = \frac{(x, y)}{h}, \quad (U, V) = \frac{(u, v)}{u_{\text{in}}}, \quad \tau = \frac{u_{\text{in}}}{h} t \tag{12}$$

$$C = \frac{c - c_0}{c_{\text{in}} - c_0}, \quad K = \frac{k}{u_{\text{in}}^2}, \quad E = \frac{\nu}{u_{\text{in}}^4} \varepsilon \tag{13}$$

$$P = \frac{p}{\rho u_{\text{in}}^2}, \quad Re = \frac{u_{\text{in}} h}{\nu}, \quad Sc = \frac{\nu}{\mathscr{D}} \tag{14}$$

$$Re^* = \frac{u_{\text{in}} h}{\nu_{\text{t}}} = \frac{Re}{a_2 f_2} \frac{E}{K^2} \tag{15}$$

in which on the right-hand sides we see the actual (physical) variables listed in the Nomenclature. Worth mentioning are the Reynolds number based on inlet width, $Re$, and the relationship between $Re$ and $Re^*$, equation (15). The dimensionless factors $f_1$ and $f_2$ are functions of only the turbulence Reynolds number $Re_{\text{t}}$

$$f_1 = 1 - 0.3 \exp(Re_{\text{t}}^2) \tag{16}$$

$$f_2 = \exp\left[\frac{-2.5}{1 + Re_{\text{t}}/50}\right] \tag{17}$$

$$Re_{\text{t}} = \frac{k^2}{\nu \varepsilon} = \frac{K^2}{E}. \tag{18}$$

For the numerical constants required by this model we followed Patankar *et al.*'s [3] approach, and used all the values proposed by Jones and Launder [1] except the turbulent Schmidt number

$$a_k = 1.44, \quad a_1 = 1.92, \quad a_2 = 0.09$$
$$\sigma_K = 1, \quad \sigma_E = 1.3. \tag{19}$$

In the present study, we fine-tuned the value of the turbulent Schmidt number $\sigma_C$ by comparing the numerical results with actual experimental data, as described in Section 4. Worth noting is that Jones and Launder's method [1] extends the standard $k$–$\varepsilon$ model to the low Reynolds number form, allowing in this way a solution of the flow equations that holds all the way to the wall. Consequently, there is no need for 'wall functions' to account for the large damping of the turbulence in the wall region.

The dimensionless form of the initial and boundary conditions is indicated in the lower part of Fig. 1. All the solid surfaces are modelled as impermeable with no slip. The flow through the inlet port is purely horizontal (forming a wall jet along the ceiling), and

the velocity and concentration of this stream are uniform over the cross-section of the inlet port. The inlet values of the dimensionless $K$ and $E$ are based on the assumption of fully developed turbulent flow in which $k$ represents 1% of the mean kinetic energy, and where the representative mixing length is of the order of 5% of the inlet width $h$

$$K_{in} = 0.01, \quad E_{in} = \frac{0.02}{Re}. \tag{20}$$

We found, however, that the numerical results are order-of-magnitude insensitive to changes in the assumed values of $K_{in}$ and $E_{in}$ (Table 1). Listed in the last column is the dimensionless concentration decay time defined later in equation (26).

The outlet conditions are less evident, as their selection depends to a certain degree on the numerical method. Based on the tests discussed later in connection with Fig. 2(c), we chose the conditions shown in Fig. 1, namely zero diffusion of $C$, $K$ and $E$ across the outlet plane.

The shape of the enclosure and the relative size of the two ports (one inlet, one outlet) were fixed

$$\frac{L}{H} = 2, \quad \frac{h}{H} = 0.1. \tag{21}$$

As an alternative to the dimensionless time $\tau$ defined in equation (12), it is worth noting the new volume replacement time

$$\tau^* = \frac{t}{LH/u_{in}h}. \tag{22}$$

The quantity in the denominator represents the time in which the inlet stream can fill the enclosure volume once. The proportionality between the dimensionless times $\tau^*$ and $\tau$ is

$$\frac{\tau^*}{\tau} = \frac{h^2}{LH} \tag{23}$$

or, according to equations (21), $\tau^* = 0.005\tau$. The gradual removal of the contaminant from the enclosure was monitored by calculating the 'displacement efficiency' introduced in ref. [4]

$$\eta_d = \frac{\bar{c} - c_0}{c_{in} - c_0} = \bar{C} \tag{24}$$

in which the overbar indicates a total-volume average.

Table 1. The effect of the inlet turbulence kinetic energy and the representative mixing length ($Re = 5000$)

| $K_{in}$ | $E_{in}Re$ | $\tau_c^*$ |
|---|---|---|
| 0.01 | 0.02 | 267.1 |
| 0.05 | 0.22 | 266.4 |
| 0.05 | 0.11 | 268.3 |

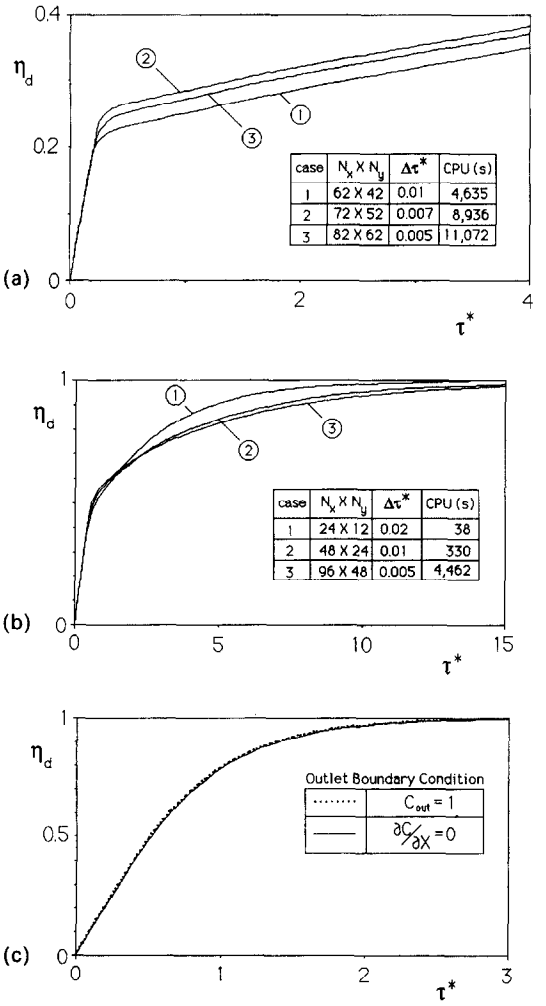


FIG. 2. Numerical accuracy tests: (a) the effect of grid size and time step for high-$Re$ flow ($Re = 5000$); (b) the effect of grid size and time step for low-$Re$ flow ($Re = 30$); (c) the effect of the outlet boundary condition on ventilation efficiency ($Re = 5$).

## 3. NUMERICAL METHOD

The equations described in the preceding section were solved numerically using the SIMPLE algorithm described in detail by Patankar [5]. The quadratic upstream-weighted differencing method of Leonard [6] was used in order to minimize the effect of numerical diffusion. Following Leschziner and Rodi [7], we applied the power-law method of Patankar [8] to the $k$–$\varepsilon$ equations (5) and (6), because these equations are less sensitive to the discretization method.

Underrelaxation was used in the solving of the nonlinear equations, by following the procedure described by Van Doormaal and Raithby [9]. In the case of low Reynolds numbers and laminar flow, their improved SIMPLEC algorithm resulted in a considerably faster convergence. At the higher Reynolds numbers considered in this study, there was no distinct advantage in using the SIMPLEC algorithm, because in that range the pressure gradient is no longer a dominant term in the momentum balance.

At every time step the system of six algebraic equations was solved on a line-by-line basis using the Tridiagonal Matrix Algorithm (TDMA). This process was repeated until the solution converged. The convergence criterion was a global one based on the relative incremental changes in the displacement efficiency

$$\frac{\eta_d^{j+1}-\eta_d^j}{\eta_d^j} < 10^{-6}. \quad (25)$$

The convergence was improved using the additive-correction method described in Settari and Aziz [10].

The numerical results reported in this paper were obtained using the Cornell National Supercomputer Facility (CNSF) mainframe, which is an IBM 3090-600F computer. The code was highly vectorized in order to reduce the CPU time, especially while solving the higher Reynolds number cases. Preliminary tests showed that a substantial amount of CPU time was spent on solving the system of algebraic equations. Although efficient, the TDMA algorithm inherits a strong interdependence, which inhibits the attempt to fully vectorize it. A parallel algorithm was implemented for solving the algebraic system during the most extreme (highest $Re$) runs. For this, Wang's [11] partition method was chosen, because of its simplicity and efficiency. Its use, however, was restricted to the range $Re > 3000$, in which the CPU time overhead was compensated by a meaningful reduction in the wall-clock time spent.

The numerical grid was orthogonal and nonuniform, with its lines spaced according to the power law $s_{i+1} = s_i + \alpha^i \Delta$, in which $\Delta$ is the size of the first line-to-line spacing (near the boundary), $i$ the line number, and $\alpha$ (a constant greater than 1) the grid stretching rate. The appropriate grid spacing and time step were selected based on accuracy tests of the kind exhibited in Fig. 2. The first of these, Fig. 2(a), corresponds to the highest Reynolds number considered in this study ($Re = 5000$). The molecular Schmidt number was equal to 1. The turbulent Schmidt number was set equal to 0.7, based on the experimental information discussed in the next section. Figure 2(b) shows a similar test for laminar flow ($Re = 30$) and a molecular Schmidt number equal to 10. The numerical results assembled in Sections 4 and 5 were obtained using the $82 \times 62$ grid.

The test of Fig. 2(c) confirms that the choice of the outlet boundary condition (zero flux, Fig. 1, bottom) has no effect on the central engineering result of this study. This test was conducted at the low-Reynolds number end of this study ($Re = 5$), because only in this limit is the outlet boundary condition expected to have some influence on the concentration field situated upstream. The zero mass flux condition, $\partial C/\partial X = 0$, was compared with a most unrealistic outlet condition, namely that of an outlet concentration equal to the concentration present in the inlet stream, $C_{out} = 1$. In conclusion, the change in the outlet boundary condition causes an insignificant change in the calculated ventilation efficiency. This change is even less significant in the cases documented in the present study, because the Reynolds numbers are considerably larger than 5, and the outlet concentration is always less than 1 (note that the actual $C_{out}$ is always of the same order as the enclosure-averaged concentration $\bar{C}$). The outflow zero-mass-flux condition has been used in studies of forced convection mass transfer, for example, in refs. [12, 13].

Regarding our choice of basing the turbulent flow calculation on the Jones and Launder model [1], it is worth recalling that in high-$Re$ recirculating flows the turbulent shear stress and the degree of anisotropy between the normal stresses become sensitive to the curvature of the shear layer [14]. As a more complex alternative to Jones and Launder's model, we also used Hanjalic and Launder's model [15] with the modifications proposed by Leschziner and Rodi [7], however the calculated $\eta_d$ curve was nearly identical to the one based on the much simpler Jones–Launder model. This finding is due to the relatively low Reynolds number range of this study ($Re \leqslant 5000$), and the fact that the displacement efficiency $\eta_d$ is a global parameter, which is relatively insensitive to local changes in the concentration field.

## 4. THE FLOW AND CONCENTRATION FIELDS

In view of the range covered by the mass diffusivity of gases in air at 25°C and 1 atm, the molecular Schmidt number was set equal to 1 throughout the calculations performed in this study. The value of the turbulent Schmidt number (assumed constant) was set at 0.7 after comparing the numerical solution for $Re = 1000$ with the corresponding experimental measurements reported in ref. [4]. The longitudinal cross-section through the three-dimensional experimental apparatus [4] was nearly the same as that of the rectangular enclosure of Fig. 1 with the relative dimensions of equations (21). The best agreement between the numerical and experimental data occurs when the turbulent Schmidt number $\sigma_C$ is equal to 0.7 (note that this value lies between the constant 0.5 associated with jet flow and 0.9 the value found in boundary layers and duct flows). When the turbulent Schmidt number is 0.7 and $\tau^* = 1$, the calculated $\eta_d$ values are 0.69 for the 'floor return' configuration, and 0.71 for the 'ceiling return' configuration. These numerical $\eta_d$ values are 6.7% lower than the experimental values of 0.74 and 0.76, respectively.

A related comparison is presented in Fig. 3, where plotted on the ordinate is the difference between the inlet concentration ($C_{in} = 1$) and the concentration averaged over the outlet cross-section ($\bar{C}_{out}$) for $Re = 1000$. The two pairs of curves correspond to the floor-return and ceiling-return configurations indicated on the figure: note that unlike in Fig. 1, in the two cases of Fig. 3 the inlet stream is oriented downward into the enclosure. The agreement between these 'local' numerical and experimental results is

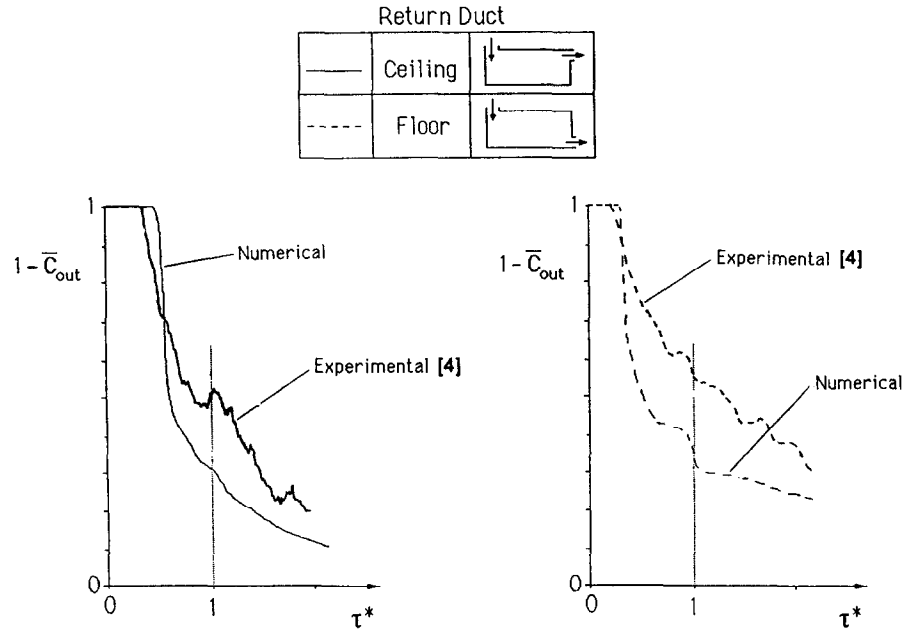


FIG. 3. The history of the calculated outlet concentration, next to the experimental curves of ref. [4] ($Re = 1000$).

quite good, considering the rough character of the two-dimensional turbulence model next to the three-dimensional water experiment (observe the crossing of the floor-return and ceiling-return curves, and the wavy shape of all the curves). Furthermore, in the experiment the step change in inlet concentration occurred after the steady-state flow was established. In the present numerical simulations the change in inlet concentration coincides with the start of the through-flow.

In Fig. 4, we see the evolution of the flow and concentration patterns when the inlet and outlet flows are both parallel to the ceiling of the enclosure. The Reynolds number is the highest considered in this study, $Re = 5000$. The flow pattern reaches its steady state at a time $\tau^*$ of approximately 2, i.e. after enough time so that the inflow of clean fluid could have filled the enclosure twice. The numbers listed next to the streamlines represent the values of the dimensionless streamfunction $\Psi$ defined by writing $U = \partial\Psi/\partial Y$ and $V = -\partial\Psi/\partial X$.

The sequence of constant-concentration lines on the right-hand side of Fig. 4 shows the manner in which the new fluid replaces the original (contaminated) fluid of the enclosure. In the first phase of this process ($\tau^* < 0.4$), the only region that is affected by the new fluid is the upper layer contained between the inlet and outlet ports. Sandwiched between this upper layer and the bulk of the fluid is a thin concentration boundary layer. The contaminant is removed gradually from the lower part of the enclosure by the slow recirculation flow and the associated mass transfer that takes place across the concentration boundary layer.

Unlike the flow field, the concentration field does not reach a steady state, except in the $\tau^* \to \infty$ limit when $C \to 1$ everywhere. The numbers listed on the constant-concentration lines in Fig. 4 represent the values of the dimensionless concentration $C$ defined in the first of equations (13). Low $C$ values correspond to contaminated fluid, while $C$ values close to 1 represent flow regions that have been effectively cleaned by the through-flow. Worth noting is that the region that is the last to be cleansed of contaminated fluid coincides with the central zone of the slow clockwise recirculation illustrated by the streamline patterns in the steady state.

In Fig. 5, we see the changes that occur in the flow and concentration fields when the outlet port is moved down to the floor level (indirect flow, or floor return, Fig. 1). In this case the inlet and outlet ports are diametrically opposed, and the main 'fiber' of the through-flow (the jet) is forced through a larger volume of the enclosure. The single recirculation cell of Fig. 4 is now divided into three, clearly demonstrating that exit port location can have a dramatic effect upon local concentrations during transient contaminant removal. In the next section we show that this 'fragmentation' of the enclosure fluid translates into a greater ventilation efficiency, that is greater than the corresponding $\eta_d$ value of the 'straight through' flow arrangement of Fig. 4.

At lower Reynolds numbers, the jet chooses a path that comes closer to the geometric center of the enclosure. This change becomes evident as we compare the left-hand side of Fig. 5 with the left-hand side of Fig. 6. In the latter, the Reynolds number is very low ($Re = 30$), and the flow is laminar [16]. The jet divides

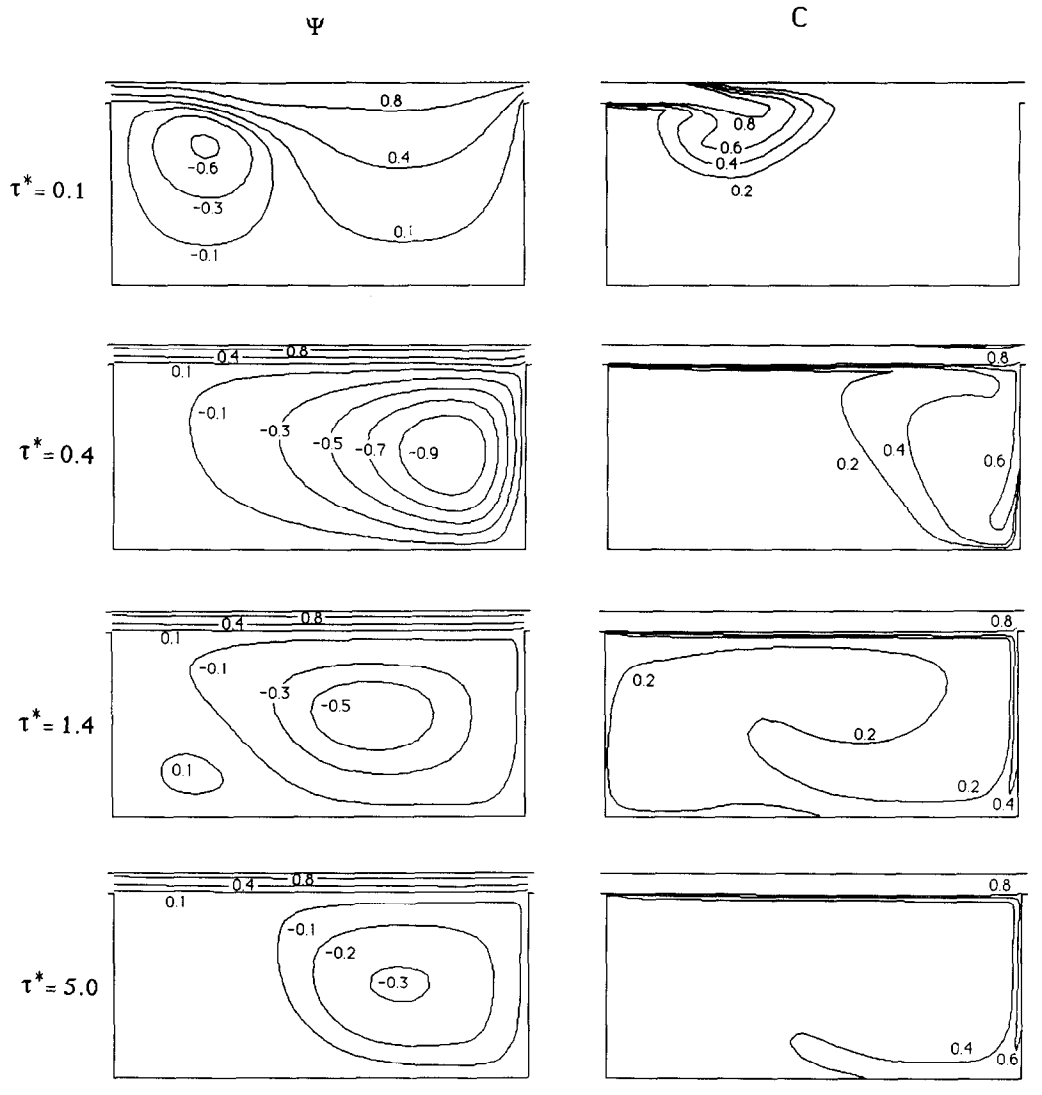


FIG. 4. The evolution of the flow and concentration patterns when the inlet and outlet ports face each other ($Re = 5000$).

the enclosure into two large corner cells, such that the clockwise one (in the lower-left region) is stronger. The constant-concentration lines reveal a contaminant removal process in which the contaminated fluid (small $C$ values) is displaced to the right, in piston-like fashion.

## 5. THE DISPLACEMENT EFFICIENCY

Figure 7 shows the effects of time, Reynolds number and outlet location on the displacement efficiency $\eta_d$. The local volume displacement decreases with time, however, in the turbulent range ($Re \gtrsim 10^2$) this decrease has two distinct phases. There is an early phase in which $\eta_d$ increases rapidly and is in fact independent of the Reynolds number. We show in the next section that this early phase corresponds to the time in which the new fluid travels directly between the inlet and outlet ports, filling the imaginary duct (the jet region) that connects the two ports. The contaminant removal process in this phase is similar to the action of a piston (see the small-$\tau^*$ frames on the right-hand sides of Figs. 4 and 5), and resembles the mechanism seen in laminar flow (Fig. 6). This is why in the early phase $\eta_d$ is independent of $Re$.

In the phase that follows, the contaminant removal process is governed by the mass transfer across the turbulent shear layers formed between the through-flow (the jet) and the surrounding fluid. The slope of $\eta_d$ vs $\tau^*$ in this regime is considerably smaller, and continues to decrease as $Re$ increases.

The two frames of Fig. 7 are intended to show also the effect of the position of the outlet port, specifically that in the case of indirect flow (floor return) the efficiency is greater than in the case of direct flow (ceiling return). The effects of Reynolds number and flow configuration can be discussed quantitatively by defining the critical (or clean-up) dimensionless time

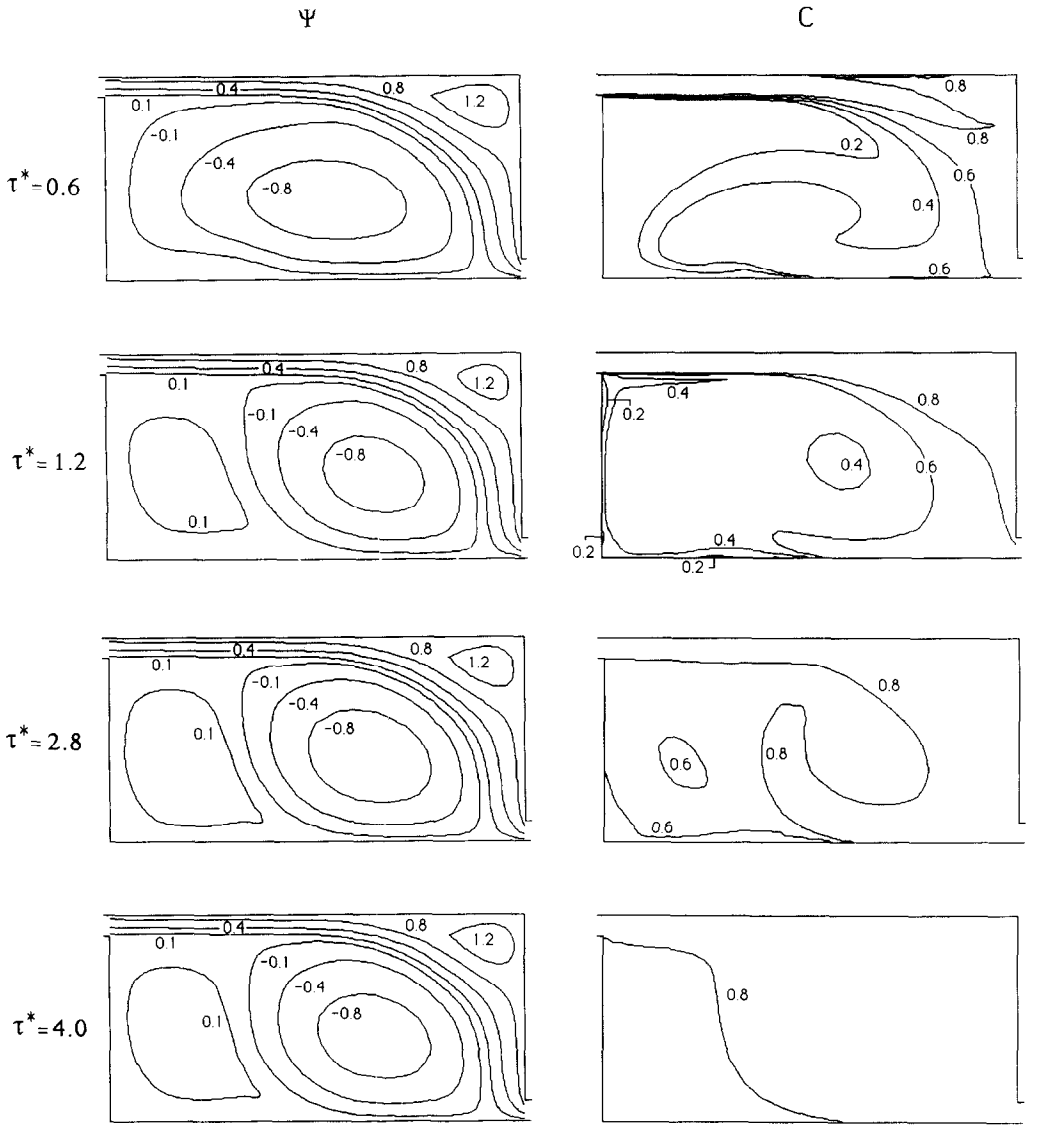


FIG. 5. The evolution of the flow and concentration patterns when the inlet and outlet ports are located in diametrically opposite corners ($Re = 5000$).

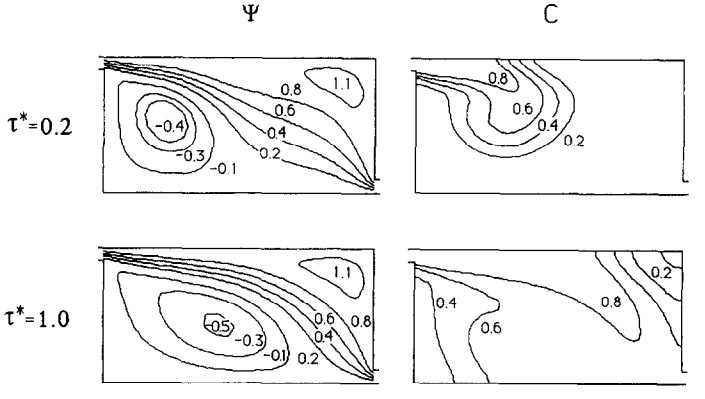


FIG. 6. Laminar flow: the evolution of the flow and concentration patterns when the inlet and outlet ports are located in diametrically opposite corners ($Re = 30$).

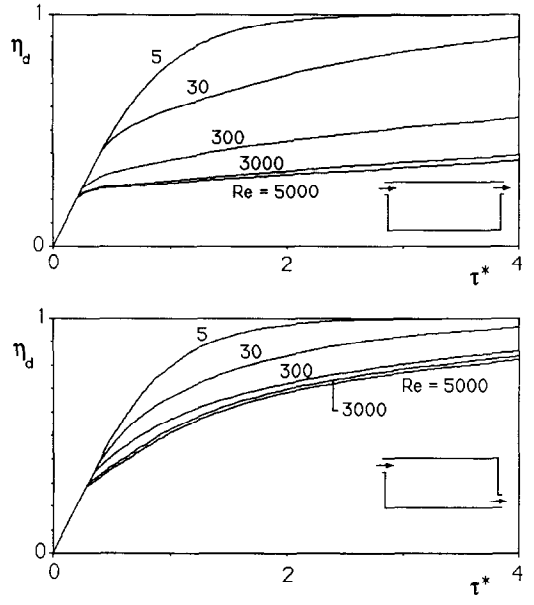


FIG. 7. The effects of time, Reynolds number and flow configuration on the ventilation efficiency.

$\tau_c^*$ when the ventilation efficiency is within 0.001% of its ultimate (infinite time) value

$$\eta_d(\tau_c^*) = 0.99999. \tag{26}$$

The $\tau_c^*$ values calculated in this manner are summarized in Fig. 8, showing that, indeed, it takes longer to remove the contaminant when the inlet and outlet ports face each other. This effect of the relative positioning of the ports is particularly noticeable at high Reynolds numbers: at $Re = 5000$, the critical dimensionless time of the direct flow arrangement is almost ten times greater than the $\tau_c^*$ value of the indirect flow configuration.

Figure 8 shows also that the laminar and turbulent portions of each $\tau_c^*$ vs $Re$ curve are fitted well by curves of the type

$$\tau_c^* = A\,Re^m. \tag{27}$$

The appropriate empirical constants $A$ and $m$ are presented in Table 2. The fact that the exponent $m$ is consistently less than 1 means that the actual time, $t_c$ (seconds), that corresponds to $\tau_c^*$ decreases as $Re$ increases (i.e. contrary to the impression left by Fig. 8, in which $\tau_c^*$ increases with $Re$)

$$\tau_c = \frac{\tau_c^*}{Re}\frac{HL}{\nu}. \tag{28}$$

For example, if in the direct-flow configuration $Re$ increases from 30 to 3000, the actual critical time $t_c$ decreases by a factor of 6.9. In the indirect-flow configuration, $t_c$ decreases by a factor of 20.7.

Table 2. Empirical constants for the critical dimensionless time correlation (27), Fig. 8

| | Laminar flow | Turbulent flow |
|---|---|---|
| Direct flow | $A = 1.221$<br>$m = 0.739$ | $A = 10$<br>$m = 0.385$ |
| Indirect flow | $A = 1.893$<br>$m = 0.468$ | $A = 12.87$<br>$m = 0.155$ |

In view of the above observation, it was tempting to replot Figs. 7 and 8 using the real time ($tv/HL$) instead of $\tau^*$. We were unable to follow this course because $tv/HL$ is the same as $\tau^*/Re$, and, with $Re$ varying from 5 to 5000, it would have meant the loss of clarity ('correlation') in the graphic presentation of the curves. In Fig. 7, for instance, only one or two of the curves would have fit inside the frame of the drawing.

The effect of flow configuration is documented further in Fig. 9. The two lower curves represent the configurations discussed already, direct flow and indirect flow. New in this figure are the upper curves, which correspond to flows where the inlet and outlet streams are oriented perpendicularly (as in Fig. 3). In this way we discover that:

(1) the relative perpendicular orientation of the inlet and outlet ports yields a substantial increase in displacement efficiency;

(2) the effect of outlet location is reduced dramatically when the inlet and outlet port cross-sections are perpendicular.

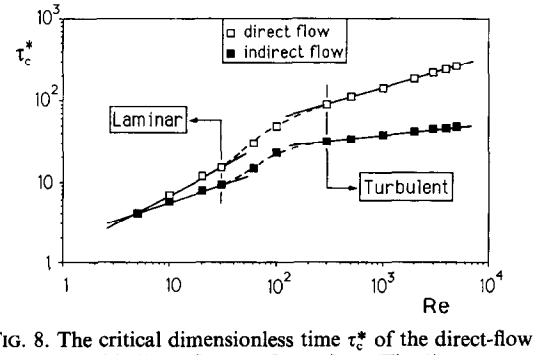


FIG. 8. The critical dimensionless time $\tau_c^*$ of the direct-flow and indirect-flow configurations (Fig. 1).

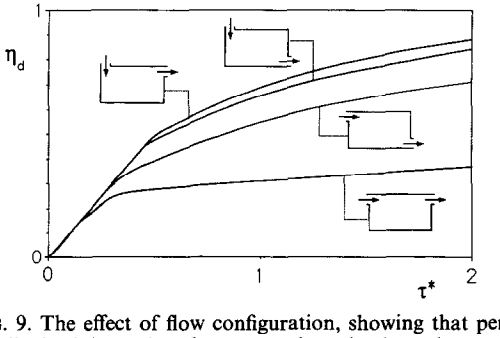


FIG. 9. The effect of flow configuration, showing that perpendicular inlet and outlet ports reduce the dependence on outlet location, and increase the displacement efficiency ($Re = 1000$).

It is interesting that the highest ventilation efficiency is achieved when the ports are perpendicular and on the same side of the enclosure (ceiling in Fig. 9). This is the opposite of what we found when the inlet and outlet cross-sections are parallel, where the diametrically opposed ports yield the greater $\eta_d$ (Fig. 7). Since $\eta_d$ is a measure of the volume fraction that has been replaced by 'new' air (i.e. air that entered the enclosure after $\tau = 0$), the difference $(1-\eta_d)$ is proportional to the volume fraction that has short-circuited directly to the outlet, without replacing the original air that filled the enclosure at $t = 0$.

## 6. THEORETICAL CONSIDERATIONS

For the purpose of environmental design calculations, it is useful to condense these numerical ventilation efficiency curves into simple analytical expressions of the type $\eta_d(\tau^*, Re, \text{flow configuration})$. The analytical form of these expressions can be anticipated theoretically. Three possible models are sketched in Fig. 10.

In the first model, it is assumed that the new fluid ($C = 1$) displaces the contaminated fluid in piston-like fashion. This is equivalent to assuming that (a) the new and old fluids do not mix, and (b) the new fluid arrives at the outlet only after all the old fluid has vacated the enclosure. It is easy to show that under these circumstances the ventilation efficiency is given by

$$\eta_d = \begin{cases} \tau^*, & 0 \leqslant \tau^* \leqslant 1 \\ 1, & \tau^* > 1 \end{cases} \quad (29)$$

In the second model the instantaneous fluid inventory of the enclosure is perfectly mixed, so that the concentration at the outlet is exactly the same as the concentration at a point inside the enclosure. The analysis is the same as in the classical problem of batch mixing [17], and the result is that the concentration of the mixed fluid rises exponentially to the concentration of the inlet stream

$$\eta_d = 1 - \exp(-\tau^*). \quad (30)$$

One would think that these two simple models—no mixing and perfect mixing—would recommend formulas that act as upper and lower bounds for the actual $\eta_d$ value revealed by numerical simulations. Figure 11 shows that, unfortunately, both models overpredict the displacement efficiency, for all times $\tau^* > h/H$. The overprediction is dramatic at high Reynolds numbers, while the simple models do relatively better in the low $Re$ range of 5–30. The piston-flow model is successful only in the very beginning of the through-flow process, when the new fluid travels directly from the inlet to the outlet (e.g. the right-hand side of Fig. 4 at $\tau^* = 0.1$).

An alternative model is outlined at the bottom of Fig. 10. The enclosure volume is viewed as a sandwich of two regions. The upper region—the 'jet'—connects the inlet to the outlet, and has a width of the order of $h$. Only in this region does the new fluid displace the contaminated fluid in piston-like fashion. The jet region becomes filled completely with new fluid at a time $t$ of the order of $L/u_{in}$, which corresponds to the dimensionless time $\tau^* \sim h/H$. It is easy to see that at times $\tau^*$ shorter than $h/H$, this new model is equivalent to the piston-flow model discussed first, therefore the displacement efficiency is

$$\eta_d = \tau^* \quad (\tau^* \leqslant h/H). \quad (31)$$

At times $\tau^* > h/H$, the jet region is inhabited by new fluid ($C = 1$). It is assumed that the remaining (lower) volume of the enclosure—the 'roll'—contains fluid that is well mixed by the recirculating flow en-

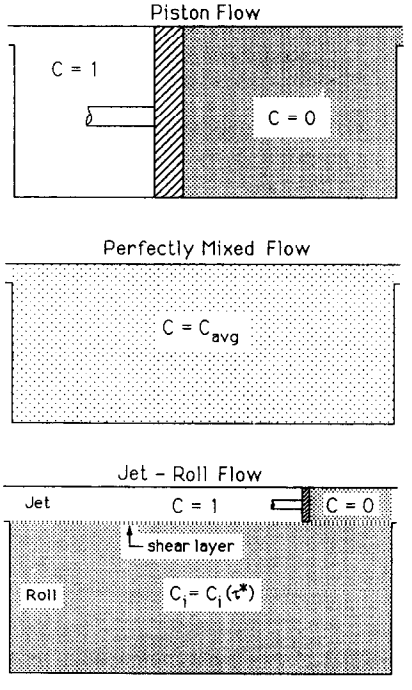


FIG. 10. Three simple models for determining the ventilation efficiency function $\eta_d(\tau^*)$.

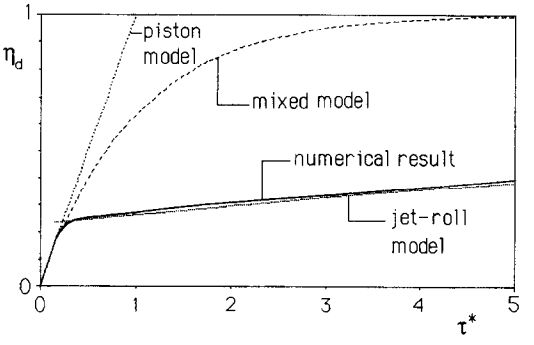


FIG. 11. Comparison between the numerical $\eta_d$ results and the predictions based on the models of Fig. 10 ($Re = 5000$, direct flow).

countered in Figs. 4–6. The instantaneous dimensionless concentration in this lower region is time-dependent, $C_i(\tau^*)$. This concentration increases in time because of the mass transfer that takes place across the turbulent shear layer that separates the jet region from the roll region (Fig. 10, bottom). The existence of this turbulent shear layer was already noted while examining the right-hand side of Fig. 4 (e.g. $\tau^* = 1.4$), which shows clearly a thin concentration boundary layer between the jet and the roll.

It is assumed finally that the mass transfer rate across the jet–roll concentration boundary layer is proportional to the instantaneous jet–roll concentration difference $(1-C_i)$. Taking into account the geometry of the enclosure, we write that the conservation of species (contaminant) in the roll region of height $(H-h)$ and length $L$ requires

$$L(H-h)\frac{dC_i}{dt} = b_1 L(1-C_i) \tag{32}$$

in which the factor $b_1$ accounts for the effective mass eddy diffusivity in the boundary layer region. This factor will be determined empirically.

In the search for the counterpart of the $\eta_d$ expression (31) in the limit $\tau^* \to \infty$, we integrate equation (32) from the beginning ($C_i = 0$ at $\tau^* = 0$)

$$C_i = 1-\exp\left[-\frac{LH}{h(H-h)}\tilde{b}_1\tau^*\right] \tag{33}$$

by writing $\tilde{b}_1$ for the dimensionless empirical factor that corresponds to $b$. Next, we note that the ventilation efficiency $\eta_d$ is equal to the concentration averaged over the entire volume (jet + roll)

$$\eta_d = \frac{h}{H} + \frac{H-h}{H}C_i \tag{34}$$

and arrive in this way at the expression

$$\eta_d = 1-\left(1-\frac{h}{H}\right)\exp\left[-\frac{LH}{h(H-h)}\tilde{b}_1\tau^*\right]. \tag{35}$$

Finally, we must recognize that in the volume averaging operation executed in equation (34) the geometric factors $h/H$ and $(H-h)/H$ are correct only in an order of magnitude sense. This means that a more accurate alternative to equation (35) is

$$\eta_d = 1-\left(1-\frac{h}{H}\right)\tilde{b}_2\exp\left(-\frac{L/h}{1-h/H}\tilde{b}_1\tau^*\right) \tag{36}$$

in which $\tilde{b}_2$ is a second empirical factor whose expected order of magnitude is 1.

The contribution of the jet–roll model is that it predicts the exponential form (36), in which $\tilde{b}_1$ and $\tilde{b}_2$ are independent of time. The constancy of $\tilde{b}_1$ in time stems from the observation that the flow pattern (in particular, the turbulent shear layer) is in its steady state during most of the long-time interval ($\tau^* \gtrsim h/H$) in which equation (36) applies. This prediction is equivalent to saying that the numerical $\eta_d$ results must appear as a straight line when plotted as $\log(1-\eta_d)$ vs $\tau^*$. Figure 12 shows that this is indeed the case.

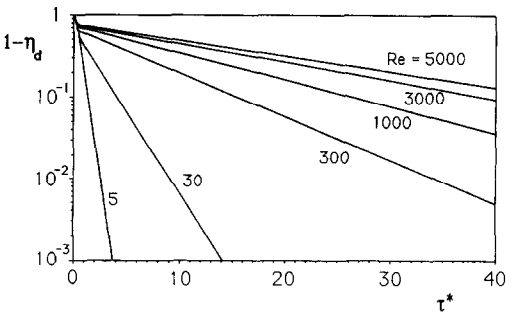


FIG. 12. Semilogarithmic plot of the numerical $\eta_d$ results for the direct-flow configuration, validating the exponential form derived in equation (36).

Figures like Fig. 12 were drawn for each flow configuration, in order to determine the $\tilde{b}_1$ and $\tilde{b}_2$ factors that lead to the best agreement between equation (36) and the numerical $\eta_d$ data. The $\tilde{b}_1$ and $\tilde{b}_2$ values were themselves curve fitted as functions of Reynolds number in the range 5–5000. The resulting expressions for $\tilde{b}_1$ and $\tilde{b}_2$ are reported in Fig. 13. Taken together, equations (31), (36) and Fig. 13 provide an analytical summary for the numerical displacement efficiency results developed in this study. Equation (36) reproduces the calculated $\eta_d$ values with an accuracy better than 4.3%, and $\tau_c^*$ with an accuracy better than 0.2%.

## 7. CONCLUSION

The present study showed that significant gains in ventilation efficiency can be achieved by properly positioning and orienting the inlet and outlet ports. The highest efficiency is achieved in geometric arrangements where the path of the jet is the longest and the short-circuiting is the smallest. The contribution of the present study relative to the experiments of ref. [4] is that it increases the *Re* range above 2000, and it allows more flexibility in the study of the effect of inlet/outlet geometry on the effectiveness of contaminant removal.

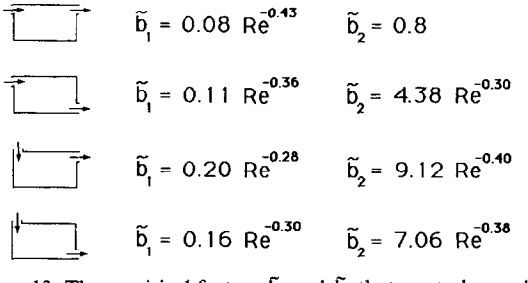


FIG. 13. The empirical factors $\tilde{b}_1$ and $\tilde{b}_2$ that are to be used in equation (36).

*Acknowledgements*—The work described in this paper was supported in part by the DOE Office of Building Technology, Division of Building Systems, John Talbott, Program Manager. The numerical work was conducted using the Cornell National Supercomputer Facility, a resource of the Center for Theory and Simulations in Science and Engineering (Cornell Theory Center), which receives major funding from the National Science Foundation and IBM Corporation, with additional support from New York State and members of the Corporate Research Institute.

## REFERENCES

1. W. P. Jones and B. E. Launder, The prediction of laminarization with a two-equation model of turbulence, *Int. J. Heat Mass Transfer* **15,** 301–314 (1972).
2. C. K. G. Lam and K. Bremnorst, A modified form of the $k$–$\varepsilon$ model for predicting wall turbulence, *J. Appl. Mech.* **103,** 456–460 (1981).
3. S. V. Patankar, E. M. Sparrow and M. Ivanovic, Thermal interactions among the confining walls of a turbulent recirculating flow, *Int. J. Heat Mass Transfer* **21,** 269–274 (1978).
4. R. Anderson and M. Mehos, Evaluation of indoor air pollutant control techniques using scale experiments, *Engineering Solutions to Indoor Air Problems, Proc. ASHRAE Conf. IAQ 88*, Atlanta, Georgia, pp. 193–208 (1988).
5. S. V. Patankar, *Numerical Heat Transfer and Fluid Flow*. Hemisphere, Washington, DC (1980).
6. B. P. Leonard, A stable and accurate convective modelling procedure based on quadratic upstream interpolation, *Comput. Meth. Appl. Mech. Engng* **19,** 59–98 (1979).
7. M. A. Leschziner and W. Rodi, Calculation of annular and twin parallel jets using various discretization schemes and turbulence-model variations, *J. Fluids Engng* **103,** 352–360 (1981).
8. S. V. Patankar, A calculation procedure for two-dimensional elliptic situations, *Numer. Heat Transfer* **4,** 409–425 (1981).
9. J. P. Van Doormaal and G. D. Raithby, Enhancement of the Simple method for predicting incompressible fluid flows, *Numer. Heat Transfer* **7,** 147–163 (1984).
10. A. Settari and K. Aziz, A generalization of the additive correction methods for the iterative solution of matrix equations, *SIAM J. Numer. Analysis* **10,** 10 (1973).
11. H. H. Wang, A parallel method for tridiagonal equations, *ACM Trans. Math. Software* 7(2), 170–183 (1981).
12. V. Hlavacek and J. Votruba, Steady-state operation of fixed-bed reactors and monolithic structures. In *Chemical Reactor Theory, a Review* (Edited by L. Lapidus and N. R. Amundson), pp. 314–404. Prentice-Hall, Englewood Cliffs, New Jersey (1977).
13. D. Schmal, J. H. Duyzer and J. van Heuven, A model for the spontaneous heating of coal, *Fuel* **64,** 963–972 (1985).
14. P. Bradshaw, Effect of streamwise curvature on turbulent flows, AGARDograph No. 169 (1973).
15. K. Hanjalic and B. E. Launder, Preferential spectral transport by irrotational straining. In *Turbulent Boundary Layers—Forced, Incompressible, Non-reacting*, pp. 101–110. ASME (1979).
16. A. J. Reynolds, Observations of a liquid-into-liquid jet, *J. Fluid Mech.* **14,** 552–556 (1962).
17. R. K. Shah and A. C. Mueller, Heat exchangers. Part 1. Heat exchanger basic thermal design methods. In *Handbook of Heat Transfer Applications* (Edited by W. M. Rohsenow, J. P. Hartnett and E. Ganic), pp. 4–60. McGraw-Hill, New York (1985).

## EFFICACITE DE L'ENLEVEMENT VARIABLE D'UN CONTAMINANT A UNE CAVITE AVEC FENTE VENTILEE

**Résumé**—On donne les résultats d'une étude fondamentale de l'enlèvement variable d'un contaminant à une cavité bidimentionnelle avec une entrée et une sortie. L'évolution des champs d'écoulement et de concentration est simulée numériquement par un modèle $k$–$\varepsilon$ de Jones et Launder pour faible nombre de Reynolds. Celui-ci varie dans le domaine 5–5000, basé sur la largeur du jet d'entrée. L'efficacité de ce mécanisme de convection forcée de masse est quantitativement décrit en fonction d'une efficacité de ventilation et d'un temps critique de décroissance de concentration. On rapporte une relation entre ces paramètres quantitatifs de performance, le nombre de Reynolds et l'orientation du jet de ventilation. On montre que le gain en efficacité de ventilation (ou une diminution du temps critique de décroissance de concentration) peut être obtenu en orientant et positionant convenablement l'entrée et la sortie l'une par rapport à l'autre et selon la cavité. Les résultats numériques de l'efficacité de ventilation sont résumés par une expression analytique compacte basée sur un modèle théorique à deux zones de l'écoulement dans la cavité.

## DIE WIRKSAMKEIT EINER ALLMÄHLICHEN ENTFERNUNG EINER VERUNREINIGUNG AUS EINEM ÜBER SCHLITZE BELÜFTETEN BEHÄLTER

**Zusammenfassung**—In der vorliegenden Arbeit wird über die Ergebnisse einer grundlegenden Untersuchung der allmählichen Entfernung einer Verunreinigung aus einem zweidimensionalen Behälter mit einem Einlaß und einem Auslaß berichtet. Die Entwicklung des Strömungs- und des Konzentrationsfeldes wird mit Hilfe des $k$–$\varepsilon$-Modells nach Jones and Launder für kleine Reynolds-Zahlen numerisch simuliert. Die Reynolds-Zahl umfaßt den Bereich von 5 bis 5000, wobei *Re* mit dem Strahldurchmesser am Eintritt gebildet wird. Die Wirksamkeit des Stofftransports durch erzwungene Konvektion wird quantitativ in Form eines Lüftungs-Wirkungsgrades und einer kritischen Zeit für das Abklingen der Konzentration dargestellt. Die Beziehung zwischen diesen quantitativen Betriebsparametern, der Reynolds-Zahl und der Orientierung des Luftstrahls wird dargelegt. Es zeigt sich, daß der Lüftungs-Wirkungsgrad dadurch verbessert werden kann (oder die kritische Zeit für das Abklingen der Konzentration dadurch verkürzt werden kann), daß die Ein- und Auslaßöffnung in geeigneter Weise angeordnet und günstig zueinander und zum Behälter ausgerichtet werden. Die numerisch berechneten Ergebnisse über den Lüftungs-Wirkungsgrad werden in einem kompakten analytischen Ausdruck zusammengefaßt, der auf einem theoretischen Zweizonenmodell der Behälterströmung aufbaut.

## ЭФФЕКТИВНОСТЬ НЕСТАЦИОНАРНОГО УДАЛЕНИЯ ПРИМЕСИ ИЗ ВЕНТИЛИРУЕМОЙ ЩЕЛЕВОЙ ПОЛОСТИ

**Аннотация**—Приводятся результаты исследования нестационарного процесса удаления примеси из двумерной полости с одним входом и одним выходом. С использованием $k$–$\varepsilon$ модели Джонса и Лондера для малых чисел Рейнольдса численно моделируется эволюция полей течения и концентрации. Число Рейнольдса $Re$, основанное на ширине входа, изменяется в интервале 5–5000. Эффективность процесса массопереноса при вынужденной конвекции оценивается на основе эффектэвности вентиляции и критического времени убывания концентрации. Анализируется взаимосвязь между этими рабочими характеристиками, числом Рейнольдса и ориентацией вентилирующей струи. Показано, что эффективность вентиляции может быть значительно повышена (или критическое время убывания концентрации может быть сокращено) при надлежащих ориентации и расположении входного и выходного отверстий по отношению друг к другу и к полости. Численные результаты для эффективности вентиляции обобщаются в виде аналитического выражения, основанного на теоретической двухзональной модели течния в полости.